FISEVIER

Contents lists available at ScienceDirect

International Journal of Heat and Mass Transfer

journal homepage: www.elsevier.com/locate/ijhmt





Heat transfer near a growing bubble during nucleate boiling using dual-tracer laser-induced fluorescence thermometry

Mahyar Ghazvini, Abel Abraham, Mazen Hafez, Myeongsub Kim

Ocean and Mechanical Engineering, Florida Atlantic University, United States

ARTICLE INFO

Keywords:
Thermal management
Nucleate boiling
Laser-induced thermometry
Temperature-sensitive dyes

ABSTRACT

Boiling heat transfer associated with bubble growth is perhaps one of the most efficient cooling methodologies due to its large latent heat during phase change. Despite the significant advancements, numerous questions remain regarding the fundamentals of bubble growth mechanisms, which is a major source of enhanced heat dissipation. This work aims to accurately measure three-dimensional (3D), space and time-resolved, local liquid temperature distributions surrounding a growing bubble to quantify the heat transfer in the superheated liquid layer during bubble growth. The dual tracer laser-induced fluorescence thermometry technique combined with high-speed imaging captures transient 2D temperature distributions, that will render 3D temperature distributions by combining multiple 2D layers, within a $0.3~^{\circ}$ C accuracy at a 30 μ m resolution. Two fluorescent dyes, fluorescein and sulforhodamine B, were used to measure transient temperatures, by account of their temperature-sensitive emissions. The results show that the temperature close to the heated surface and bubble interface exhibits an acute transient behavior at the time of bubble departure. The growing bubble works as a pump to remove heat from the surface with a peak temperature difference of up to $10~^{\circ}$ C during its growth and departure. The experimental results were compared with previously reported studies to validate the accuracy of the technique. It was found that the heat transfer coefficient close to the bubble interface and heater is approximately 1.3 times higher than the heat transfer coefficient in the bulk liquid.

1. Introduction

Thermal management of microelectronic devices has become increasingly important as their power density continues to increase, emitting excessive heat over a limited space. The extreme heat negatively impacts device performance, lifespan, and reliability [1,2]. One promising approach for managing severe heat in microelectronic devices is the utilization of nucleate boiling. Nucleate boiling occurs when a liquid is heated to its boiling point generating small vapor bubbles from a heated surface [3]. These bubbles carry heat away from the surface by phase change, enhancing cooling efficiency. Nucleate boiling effectively prevents the development of hotspots, by spreading the heat across a larger surface area, which would otherwise cause device failure or reduces system performance. Nucleate boiling also reduces thermal resistance between the microelectronic device and the cooling system, extending its lifespan [4].

To investigate nucleate boiling and associated heat transfer, transient temperature near a growing bubble must be fully characterized. Analysis of the liquid temperature distribution would allow us to design

more efficient cooling systems that can effectively manage the extreme heat. Considering the size of bubbles at a microscale, a non-invasive technique that can analyze liquid temperatures at microscale is suitable to quantify the heat transfer accurately. Dual-tracer fluorescence thermometry (DFT) offers non-invasive, transient liquid temperature measurements at a microscale [5]. The reported accuracy of DFT for temperature measurements is as small as $0.17\,^{\circ}\text{C}$ as it removes the effect of the excitation intensity (input laser light) [6]. For a given fluorophore solution at a known molar concentration C, its emission intensity (I_f) is expressed [7].

$$I_f(T) = AI_0g(T) \tag{1}$$

where A is the collection efficiency of the imaging system, I_0 is the intensity of the excitation (i.e., illumination), and g(T) depends on the quantum yield and the molar absorption coefficient of the fluorophore [8]. The temperature (T) can be obtained from the relationship between I_f and T.

DFT employs a ratiometric approach that decouples the variations in

^{*} Corresponding author.

E-mail address: kimm@fau.edu (M. Kim).

laser intensity to improve measurement accuracy—The ratio of the emissions from two different fluorophores, A and B, excited by the same illumination ($I_0^A = I_0^B$) is expressed [9]

$$I'(T) = \frac{I_f^A(T)}{I_f^B(T)} \frac{g_A(T)}{g_B(T)}$$
 (2)

Coppeta and Rogers [10] were the first to describe a ratiometric scheme and presented a comprehensive analysis of various temperature-sensitive fluorophores. They demonstrated that the ratio of signals obtained from fluorescein (Fl) and rhodamine B (RhB) enabled the accurate determination of two-dimensional mean steady-state temperature fields within a thermal plume, achieving a precision of 1.8 °C. Sakakibara and Adrian [6] employed the DFT from RhB and rhodamine 110 (Rh110) to measure water temperature, achieving an accuracy of 0.17 °C. Recently, studies on boiling phenomena using the DFT technique have helped researchers better understand heat transfer mechanisms involved in boiling. Using DFT, Tange et al. [11] investigated the temperature distribution around multiple boiling bubbles generated in a confined space. Voulgaropoulos et al. [12] employed advanced techniques, including high-speed infrared thermometry, ratiometric two-color laser-induced fluorescence, and particle image velocimetry (PIV), to investigate the bubble lifecycle in deionized water. The results revealed the contribution of evaporation at the solid-liquid-vapor contact line to bubble growth, the dynamics of the near-wall superheated liquid layer, and the quenching heat transfer process when bubbles depart from the boiling surface. Abdelghany et al. [13] used DFT thermometry to map the local and temporal temperature fields around boiling bubbles and above the heat-transfer surface using RhB and Rh110. They found that the upward movement of the vapor bubble induces the superheated liquid layer to be pulled and stretched, which is consistent with the superheated liquid layer scavenging phenomenon, as reported in the literature [2].

Despite some pioneering studies existing on temperature measurements near a growing bubble, there remains more to explore. Previous studies lack measurements of transient temperature variations at a microscale resolution near a growing bubble. Moreover, no previous studies have addressed the measurements of space- and time-resolved two-dimensional (2D) liquid temperature distributions surrounding a growing bubble, which would enable a quantitative assessment of the heat transfer from the superheated liquid layer to a vapor bubble. In this study, DFT was employed with thin film illumination to measure 2D bulk fluid temperature fields near a growing bubble within 0.3 °C at a 30 μm resolution. To visualize 3D temperature fields, multiple 2D fields

have been measured on different layers near a growing bubble. Our findings reveal an interesting transient temperature distribution during bubble departure, wherein a significant temperature drop of approximately 8–10 $^{\circ}\mathrm{C}$ occurs in the liquid near the heated surface and liquid-vapor interface.

2. Materials and methods

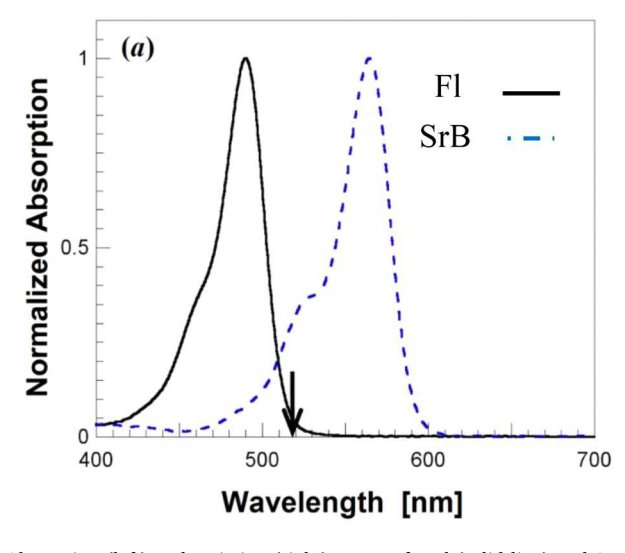
2.1. Fluorophore solution

Most temperature-sensitive fluorophores show an emission intensity that decreases with increasing temperature; this negative correlation is due to the nonradiative dissipation, which, in most cases, increases with temperature [5]. However, fluorescein (Fl) depicts a positive correlation with an emission intensity that when excited at a wavelength $\lambda=514$ nm (significantly off its absorption peak), increases with temperature [14]. Sulforhodamine B (SrB) was chosen as the second fluorophore because: (1) it can also be excited at 514 nm due to its relatively broad absorption spectrum; and (2) its emission band, with a peak at 591 nm, has little overlap with that of Fl, with a peak at 518 nm [15].

Fig. 1 shows the normalized absorption spectra (left) and the normalized emission spectra (right) as a function of wavelength at $5\mu mol/L$ Fl (solid line) and $5\mu mol/L$ SrB (dashed line) in the same deionized (DI) water [5]. The absorption spectra verify that both Fl and SrB can be excited at a wavelength of 514 nm. The emission spectra show that the fluorescence from the Fl and the SrB can be isolated from each other using appropriate emission filters—a bandpass filter (525 nm $<\lambda<555$ nm, ET540/30 m, Chroma Tech.) and a long pass filter (>600 nm, 25 mm Dia. Edmound Optics) for Fl and SrB, respectively. The effect of Fl emissions on SrB emissions (i.e., cross-talk) was no more than 0.1% of the total signal [15].

2.2. Optical system

To accurately quantify the transient local heat fluxes and 3D mapping of transient fluid temperature at a microscale spatial resolution, a thin microscale laser sheet was created. A continuous-wave (CW) aircooled argon-ion laser (Modu-Laser, Stellar-Pro-Select 150) was used to create the laser sheet, which provides multi wavelengths from 457.9 nm to 514.5 nm. The laser beam passed through an iris (10 OD, Edmundptics) to remove higher-order spatial modes and a laser excitation filter (z514/10x, Chroma Technology) subsequently to isolate the light at λ = 514 nm. The 514 nm beam is then passed through a Powell



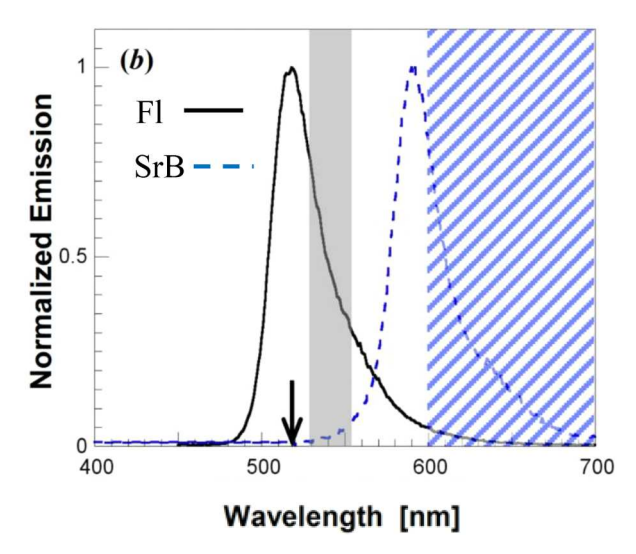


Fig. 1. Absorption (left) and emission (right) spectra for Fl (solid line) and SrB (dashed line). The arrows on both spectra indicate the excitation at 514 nm; the shaded and hatched regions on the emission spectrum denote the wavelengths transmitted by the filters that isolate the emissions from Fl and SrB, respectively [5].

lens (Edmund Optics), also known as a laser line generator lens, which diverges laser beams and creates a thin 2D laser sheet. Then, it is passed through a PCX cylinder lens (12.5 mm diameter illumination grade, Edmund Optics) to convert laser beams into uniform, straight lines. Then, the optical mirrors are adjusted to ensure that the 2D laser sheet illuminates the appropriate region of interest. Two high-speed cameras (Fastec IL5) with 2x magnification lenses and 25 frame per second and shutter speed of 40 ms are used from two sides of the boiling chamber to capture emissions of Fl and SrB near the growing bubble. Fig. 2 shows a schematic diagram of the optical system and the 2D laser sheet setup.

2.3. Fluorescence thermometry calibrations

The relationship between fluorophore's emission and temperature was calibrated in the same boiling chamber with the designed optical system at temperatures T = 20-100 °C. The temperature of the DI water in the chamber was maintained constant using a PID controller (Platinum high performance PID controller, OMEGA Engineering). In order to mitigate any potential disruption caused by dissolved air bubbles during phase-change-induced nucleation, we meticulously deaerated the DI water solution for 30 min before conducting each test. Two cartridge heaters and a K-type thermocouple and one resistance temperature detector (RTD) were immersed from the top of the solution to control and regulate the liquid temperature (Fig. 2). The pressure is atmospheric pressure, and the liquid is in subcooling state. The saturation temperature of water was considered 100 °C at atmospheric pressure. A sequence of 140 images was acquired for both the Fl and SrB emissions, respectively. After compensating for camera nonlinearities, the grayscale values were spatially averaged over a 38 \times 38 pixels (0.5 \times 0.5 mm²) region in the center of the chamber and then temporally averaged. Fig. 3 shows the average intensity, I, normalized by that at 20 °C, I_{20} , as a function of solution temperature T measured by the thermocouples at T=20–100 °C for Fl (red diamond) and SrB (green circle). The calibration for Fl and SrB were repeated and consistent over five independent experiments. The fluorescence from Fl increases by

about 2.44% per °C, based on a linear curve-fit, whereas the signal from SrB decreases by about 1.54% per °C. Both temperature sensitivities are in good agreement with the 2.43% per °C and the 1.55% per °C, reported by Coppeta and Rogers [14] for Fl and SrB, respectively. The ratio of $I_{\rm Fl}/I_{\rm SrB}$ was fitted to a polynomial function. As the order of the polynomial curve fit increases, the R^2 value may also increase. However, the increase in R^2 could be attributed to overfitting, where the model fits the noise in the data and the underlying signal, leading to poor generalization to new data. Therefore, the optimal order of polynomial curve fit depends on the balance between capturing the underlying trend in the data and avoiding overfitting. This balance can be achieved by selecting the order of polynomial that results in the highest R^2 value while minimizing the complexity of the model. Thus, in this study, the fifth-order polynomial curve fit for $I_{\rm Fl}/I_{\rm SrB}$ was selected (Figs. 4 and 5), as follows

$$T[^{\circ}C] = -0.004531 \times \overline{I}^{5} + 0.1176 \times \overline{I}^{4} - 0.9379 \times \overline{I}^{3} + 1.02 \times \overline{I}^{2} + 20.85 \times \overline{I} + 2.512$$
(3)

where T and \bar{I} are temperature and the ratio of average normalized fluorescence intensities ($I_{\rm Fl}/I_{\rm SrB}$), respectively.

We'd like to note that there would be a thermal degradation effect on fluorescence dyes, but we assume that this effect is negligible as suggested by the literature [7,16].

2.4. Fin structures

The formation of a large single bubble from a heated surface is key to accurately differentiating temperature distributions by DFT at different planes. For this purpose, we introduced a fin structure, made of copper, with a cross-sectional area 2 mm \times 2 mm and 1.5 mm height. The fin has a parabolic artificial nucleation site on the top surface, which is 500 μm deep in diameter of 300 μm on the top surface, enabling the creation of a single bubble from a heated surface as large as 1.5 mm in length, as shown in Fig. 6. The nucleation site was artificially fabricated on top of

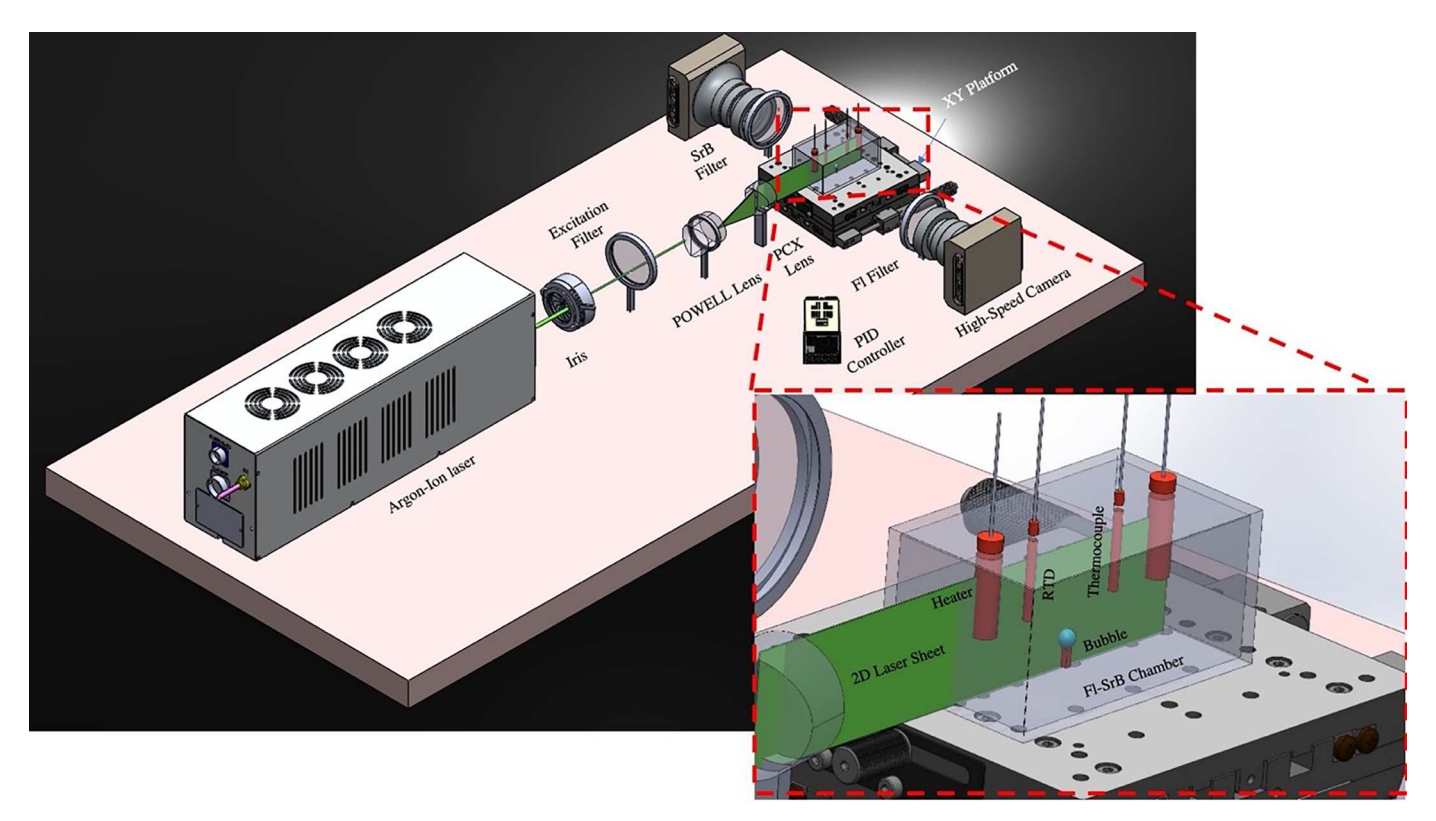


Fig. 2. The optical systems used for the DFT experiments.

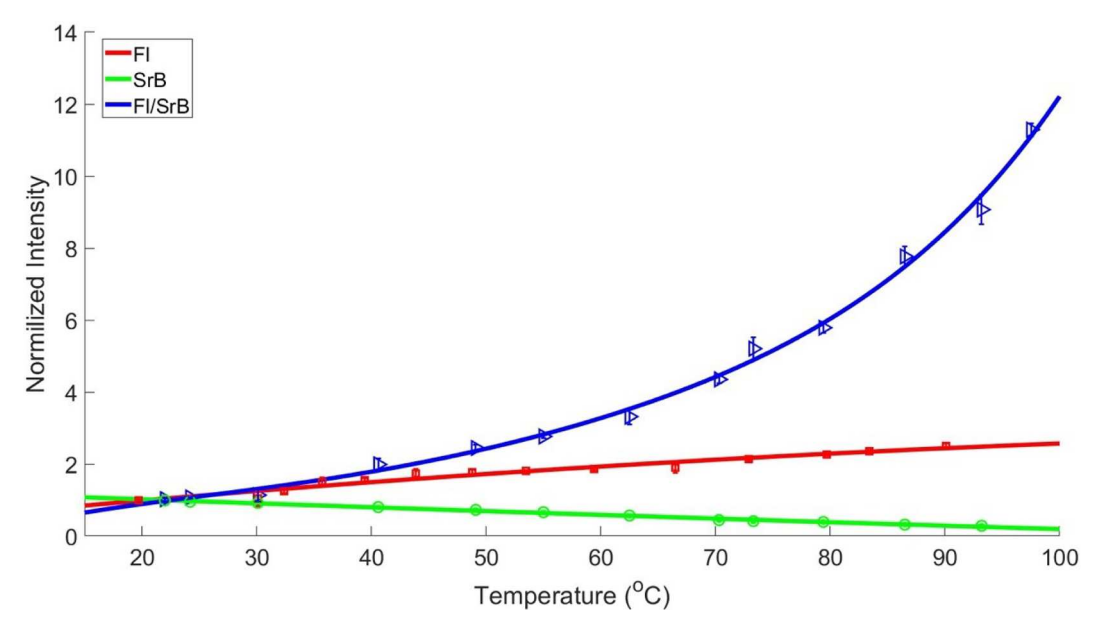


Fig. 3. An average normalized fluorescence intensity I/I_{20} as a function of solution temperature T for Fl (red diamond) and SrB (green circle). The ratio of intensities from Fl and SrB ($I_{\rm Fl}/I_{\rm SrB}$) is shown in blue triangle. (For interpretation of the references to colour in this figure legend, the reader is referred to the web version of this article.)

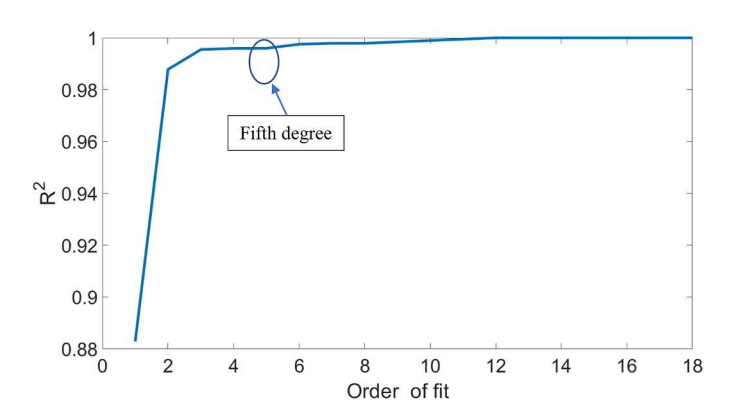


Fig. 4. A relationship between the order of polynomial curve fit and R^2 value for $I_{\rm FI}/I_{\rm SrB}$.

regular heat sinks by a milling tool. The addition of an artificial nucleation site provides a preferential location for bubble formation, which leads to more uniform and controlled bubble growth [17]. It should be noted that, due to such special arrangement on the fin structure with an

artificial nucleation site, the bubble growth process in this study might differ from that on a flat surface. The copper fin structure used in the study was obtained in the form of extruded rectangular molds with a cross-sectional area of 2 mm x 2 mm and a height of 1.5 mm. To facilitate controlled heating, we employed an insertion cartridge heater (McMaster, 400 W). A K-type thermocouple was affixed to the lower section of the heater for temperature monitoring. It's worth noting that while we conducted temperature measurements at the base of the heater, surface measurements were not the focus of our investigation as outlined in this manuscript. A 3D optical profilometer (Keyence VR-6000) was used to perform non-contact surface and roughness measurements on the fin structure at a resolution of 0.1 μm , as shown in Fig. 6.

3. Results and discussion

3.1. Transient liquid temperature distributions around a single bubble

Measuring the transient liquid temperature distribution around a single bubble, particularly in three different stages of the ebullition cycle, including initiation, growth, and departure, is crucial for understanding the heat transfer mechanisms involved in bubble growth. We

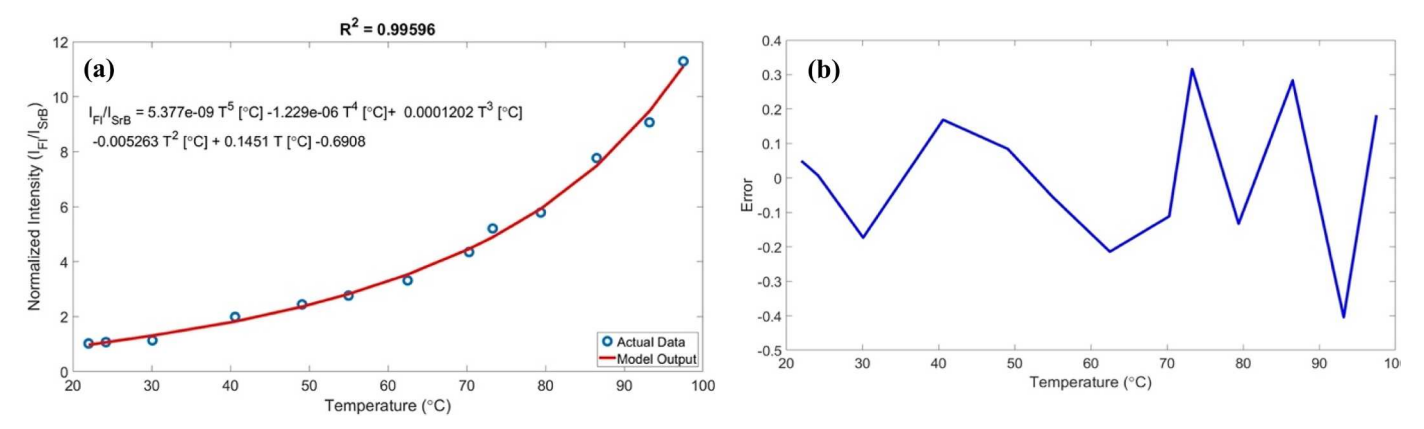


Fig. 5. (a) A fifth-order polynomial curve fit for $I_{\rm Fl}/I_{\rm SrB}$ with (b) the corresponding error (error between the fitted curve and actual data point).

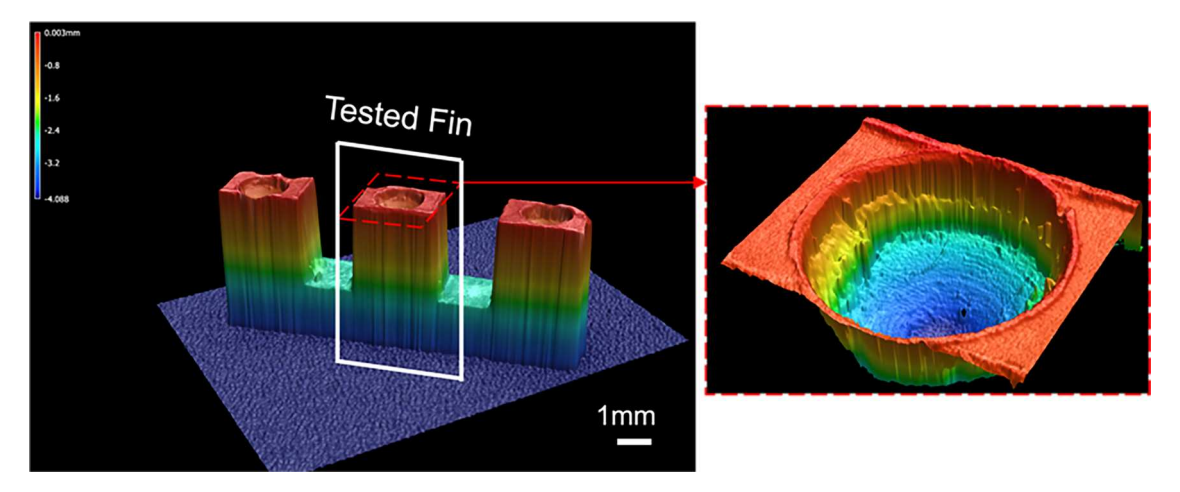


Fig. 6. 3D profiles of three fin structures with artificial nucleation sites. The white box represents the tested fin structure (i.e., a single fin) in this study. The right image is an exploded view of an artificial nucleation site.

applied the DFT technique to measure transient 2D liquid temperature for ebullition cycles. In the analysis of DFT measurements, the utilization of feature-based registration algorithm in MATLAB served as the initial step to align and match the Fl and SrB raw images, enabling precise spatial mapping and subsequent quantitative analysis of fluorescence intensity distributions. Fig. 7 shows the raw images of the bubble captured by Fl and SrB cameras.

When the surface superheat is approximately 3 °C higher than the bulk fluid temperature (i.e., $T_s - T_{bulk} \approx 3$ °C), we could observe an initiation of a single bubble. Fig. 8 shows the liquid temperature distribution surrounding the growing bubble 3 s after initiation. It demonstrates that the liquid temperature is relatively uniform at 65 °C with $a \pm 2$ °C variation from the average. This uniformity is because the bubble is small in size (~ 0.35 mm in diameter) and has just begun to form. The temperature at the liquid-vapor interface is slightly higher ($T_x = 70.4$ °C, x on Fig. 8) than the surrounding liquid, but the temperature gradient is low, 4.5 °C per 1 mm along the line indicated in the figure. The temperature distribution during initiation can be used to estimate the heat transfer rate, which is detailed in Section 3.6. The heated surface was whitened in temperature colormaps for visualization purposes. Also, the temperature measurement was not accomplished in the zone beyond the bubble (the dashed region) due to insufficient light intensity.

Fig. 9 shows the liquid temperature distribution 8–10 s after initiation during the growth stage when $T_{saturated} - T_{bulk} \approx 20$ °C, which is nonuniform. The approximate size of the bubble is 2.1 mm in diameter. The nonuniformity of temperature is primarily caused by the superheated liquid layer formed in liquid very next to the heated surface (i.e., close to y=0). The contribution of heat transfer to bubble growth increases as the superheated liquid layer expands. However, we found the

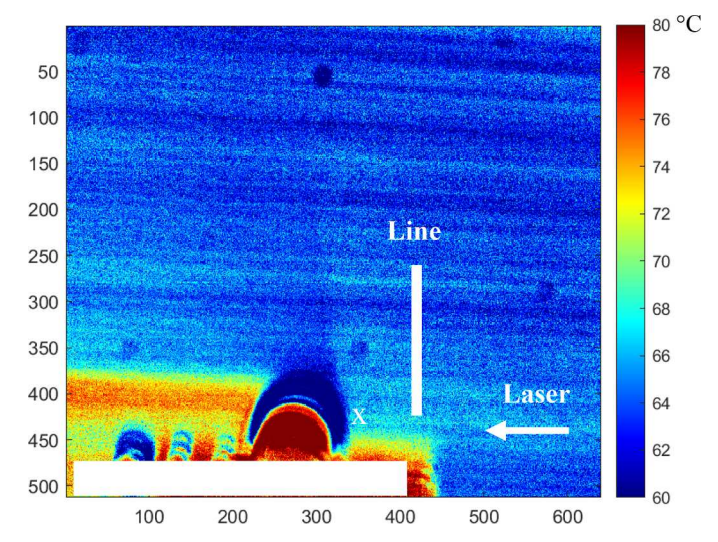


Fig. 8. Temperature colormap of a single bubble during initiation 3 s after initiation. The approximate size of the bubble is 0.35 mm in diameter.

nonuniformity in liquid temperature is dominant mainly in the early stages of bubble growth as a relatively uniform temperature distribution was observed in later stages (Fig. 9a–9c). It should be noted that the temperature at the liquid-vapor interface is close to the saturation temperature of the fluid. At the interface, liquid is in contact with the vapor phase where phase change occurs, and thus the liquid temperature

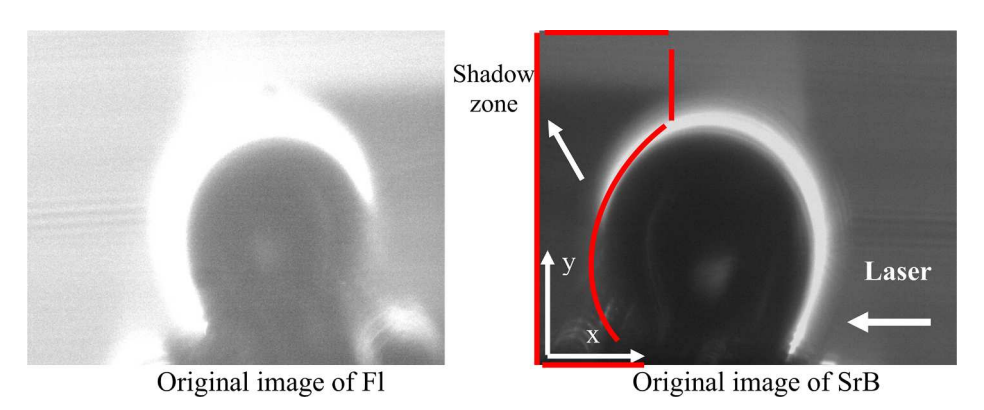
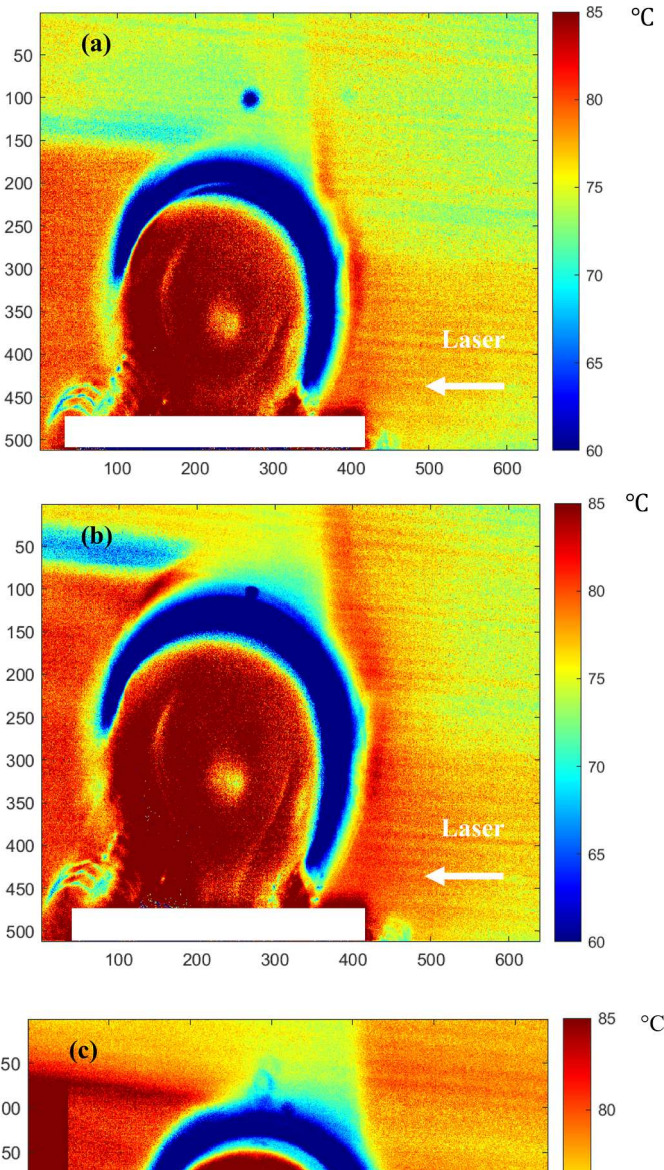


Fig. 7. Original bubble images obtained by two cameras for Fl and SrB at 5 s after initiation.



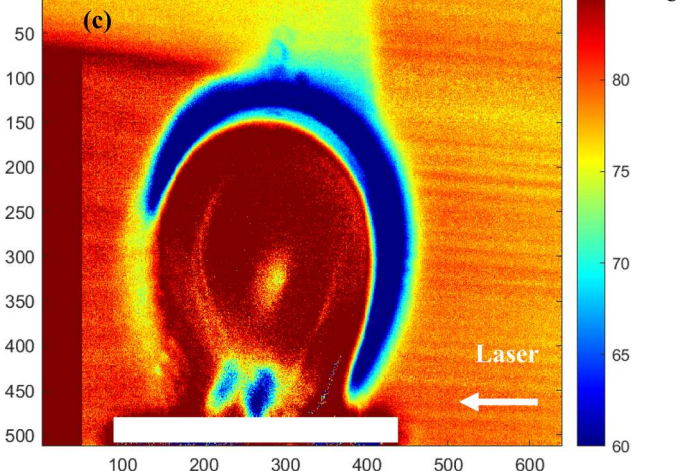


Fig. 9. Liquid temperature distributions near a bubble during growth at approximately (a) $8 \, s$, (b) $9 \, s$, and (c) $10 \, s$ after initiation. The approximate size of the bubble is $2.1 \, \text{mm}$ in diameter at $10 \, s$.

approaches the saturation temperature. Additionally, the very large heat transfer coefficient at the liquid surface significantly contributes to this effect, leading to the liquid temperature closely aligning with the temperature within the bubble, i.e., the saturation temperature.

Fig. 10 shows the liquid temperature distribution around the bubble during its departure, which is almost uniform at 82 $^{\circ}$ C, much higher than those at the bubble initiation and growth stages. This suggests that, in

the bubble departure stage, the superheated layer region is further expanded along y, and the heat transfer from this layer is generally homogeneous. We observed that, after the bubble departure, the liquid temperature close to the surface decreases due to the entrainment of colder liquid (Fig. 10c). Within a short period of time (~ 2 s), the liquid temperature distribution gradually returns to its pre-bubble state (Fig. 10d).

3.2. Transient liquid temperature distribution in three locations around a single bubble

Accurate measurements of temperature during bubble departure are of interest as bubble departure and its corresponding temperature drop directly affect the heat transfer coefficient in nucleate boiling. Furthermore, the temperature drop specifically during the departure phase remains unmeasured in literatures [18–21]. Our findings show a significant temperature drop of approximately 8–10 °C in the liquid near the heated surface and bubble interface during departure. This section details transient liquid temperature distributions at three different locations of the liquid (Fig. 11): (1) near the heated surface and the bubble interface ("1"), (2) in the middle of the bubble at the liquid-vapor interface ("2"), and in the bulk liquid away from the bubble ("3"). At each location, the temperature was averaged over a spatial resolution of 10×10 pixels, corresponding to $50 \ \mu m \times 50 \ \mu m$, at different times.

Fig. 12 shows that, at location 1, liquid temperature is relatively uniform within a 1 °C variation before bubble departure. However, as the bubble begins to detach from the heated surface, the liquid temperature close to the heated surface and the bubble interface drops rapidly due to the sudden loss of heat transfer and the influx of colder liquid. As the bubble detaches, it removes the thermal boundary layer, allowing cold liquid to come into contact with the heated surface, which further contributes to the reduction in temperature near the heated surface (Fig. 10). When a bubble detaches from the heated surface, the direct contact between the bubble and the surface is interrupted. This separation disrupts the efficient transfer of heat from the surface to the liquid, resulting in a drop in temperature [22,23]. The average temperature in the location "1" during departure differs from that of during growth (up to 10 $^{\circ}$ C). On the other hand, transient liquid temperature in the locations "2" and "3" increases as the bubble detaches from the heated surface and ascends through the liquid. This temperature rise can be attributed to the removal of the thermal boundary layer around the heated surface by the departing bubble, as well as the subsequent movement of the bubble through the liquid. This movement carries heat upward from the surface which leads to an increase in the local liquid temperature in locations "2" and "3" [24,25]. This upward movement during bubble departure is shown in Fig. 13. The maximum liquid temperature difference before and after bubble departure at locations "2" and "3" is approximately 5-7 °C when they are at approximately 350 and 900 µm away from the liquid-vapor interface, respectively.

3.4. Temperature profile along x and y

We quantified liquid temperature differences along different x and y locations during bubble growth as they provide a quantitative measure of heat transfer from liquid to the vapor bubble. Fig. 14 shows the liquid temperature distribution and associated profiles after the bubble initiation at t=10 s. The Gaussian smoothing algorithm was used to smooth out noise in temperature profiles, resulting in a smoothing effect of approximately $0.2-0.3~^{\circ}$ C in the measurements. The temperature variation at y_1 shows a sharp increase from the liquid-vapor interface toward bulk liquid, indicating significant heat transfer from the heated surface ($T_{\text{surface}} = 110~^{\circ}$ C) to the surrounding liquid ($T_{y_1=0} = 90~^{\circ}$ C). These results are consistent with the expected behavior of convective heat transfer in the vicinity of the surface. The temperature gradients at y_1 , y_2 , and y_3 locations over a 0.75 mm distance ($\Delta T/\Delta x$) are approximately 11, 6, and 5 $^{\circ}$ C, respectively, suggesting that the heat transfer rate is

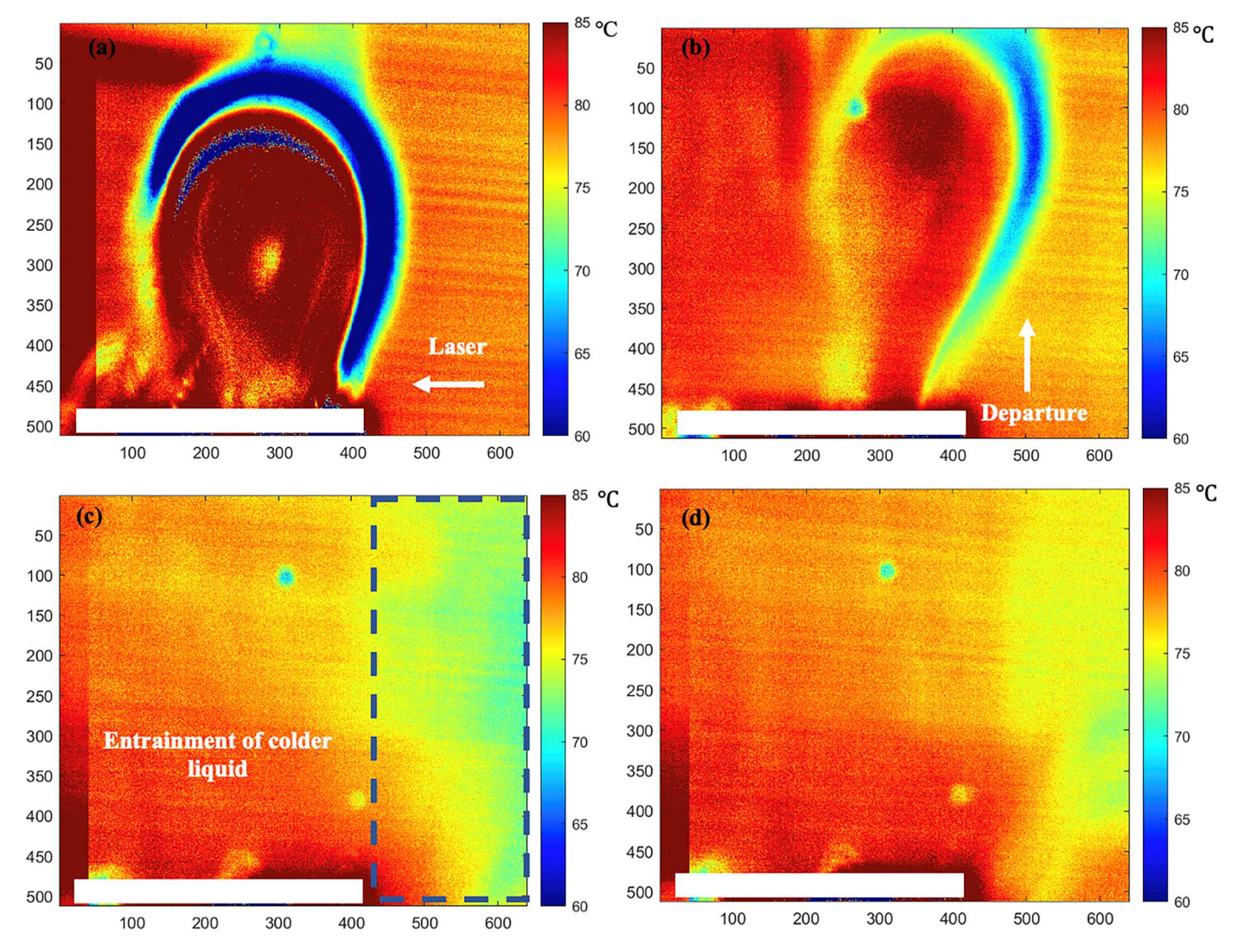


Fig. 10. (a, b) liquid temperature distribution near a bubble during departure at approximately 30 s after initiation, (c, d) liquid temperature distribution after departure at approximately 32 s after initiation. The approximate size of the bubble is 3.4 mm.

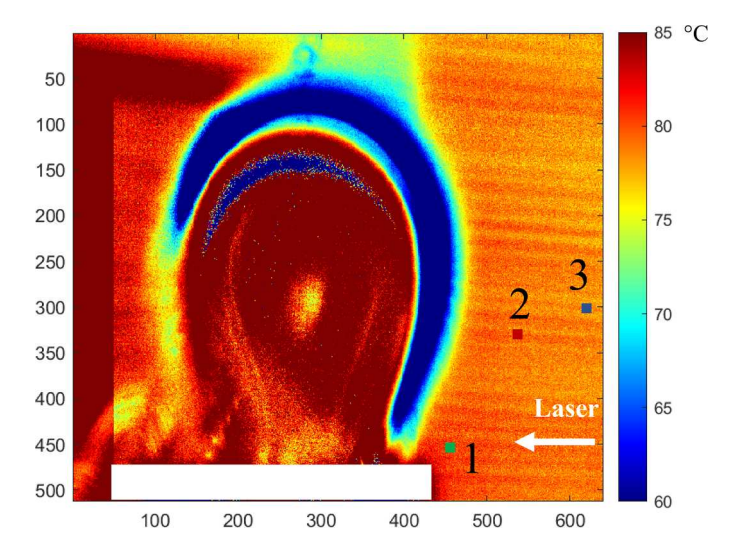


Fig. 11. A liquid temperature distribution near a bubble during departure. 1- a section of the liquid close to the heated surface and bubble interface, 2 and 3 - sections of the liquid away from the bubble.

highest at y_1 and gradually decreases at y_2 and y_3 . This indicates that the heat transfer in the liquid surrounding the bubble strongly depends on the distance from the heated surface (i.e., along y). Furthermore, the liquid temperature at three y locations approaches the bulk liquid temperature ($T=75\,^{\circ}\text{C}$), which is consistent with the conduction heat transfer in liquid away from the bubble and thermal Marangoni flow around a single bubble [26]. As the surface experiences heating, the temperature of the liquid at the bottom will exceed that of the bulk liquid. This discrepancy in temperature influences the surface tension of the bulk liquid, causing it to be greater than that of the liquid at the bottom. Consequently, a thermal Marangoni flow is initiated, transferring heat towards the bulk liquid [26].

The temperature profiles at x_1 and x_2 provide a different perspective from those at y locations. The temperature profile at different x positions exhibits a relatively constant temperature trend along y. This indicates that heat transfer in the x-direction is relatively uniform within the region of interest. However, similar to the temperature profiles observed at y locations, as we move further away from the heated surface and bubble interface, the temperature gradually decreases closer to the bulk liquid temperature. This temperature reduction is attributed to the dissipation of heat into the surrounding bulk liquid. As the distance from the heat source increases, the influence of the heated surface and bubble diminishes, leading to a convergence towards the bulk liquid temperature. Therefore, the temperature gradient at x_2 far from the interface

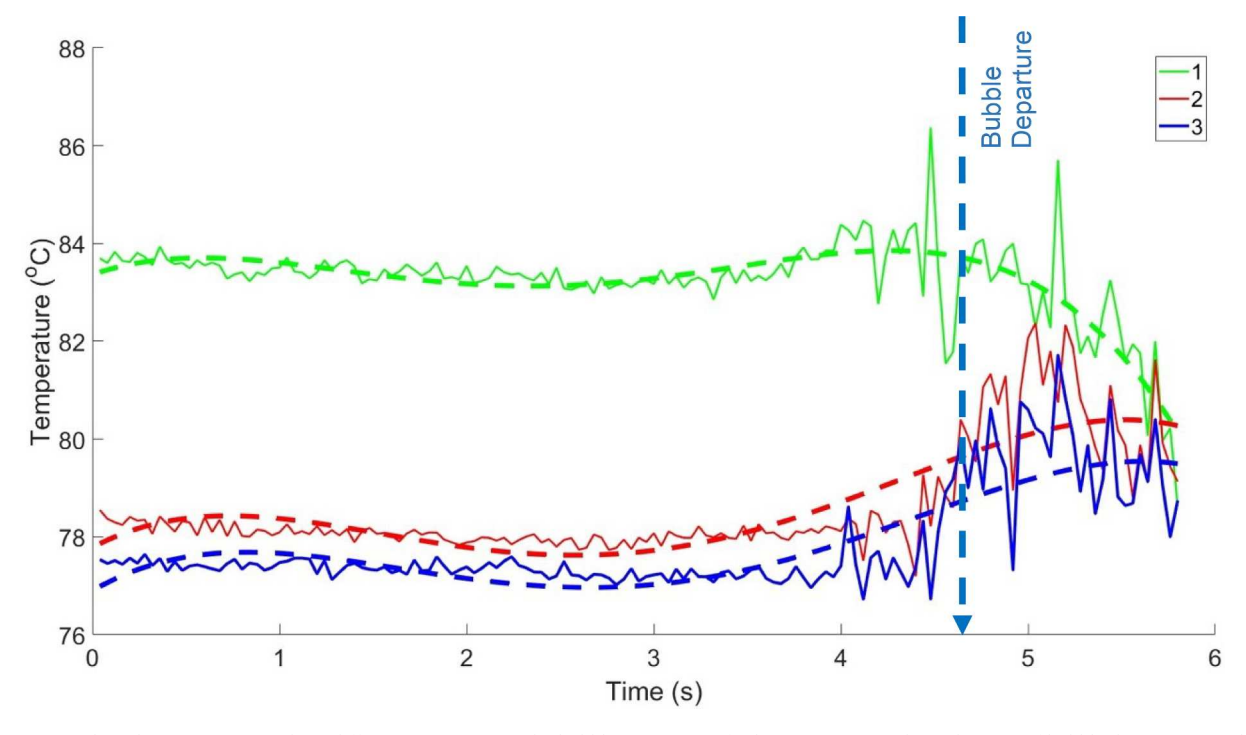


Fig. 12. Transient liquid temperature on three different sections near the bubble (see Fig. 11 for locations 1, 2, and 3). The time of bubble departure is indicated at 32 s from the initiation.

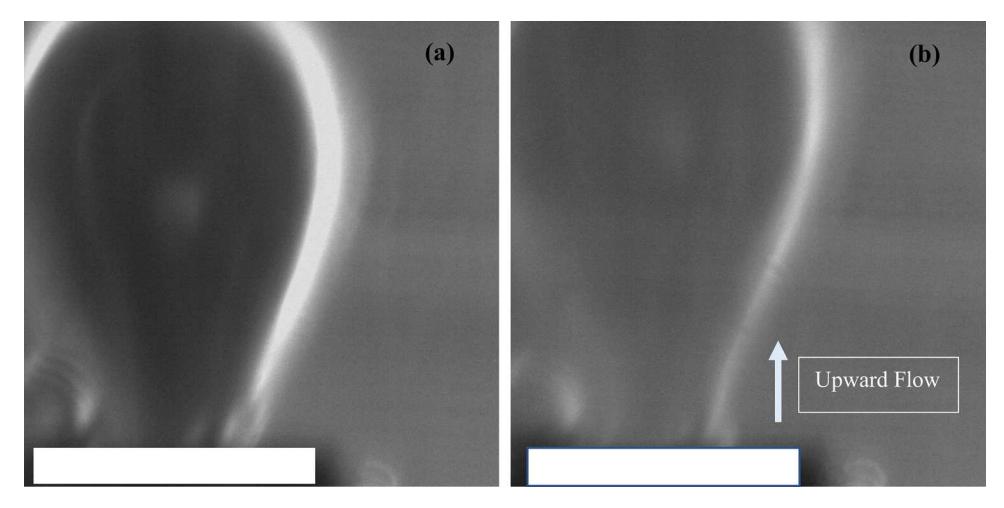


Fig. 13. Instantaneous bubble images at two subsequent times at (a) 32 and (b) 32.04 s before bubble departure.

shows a gradual decrease ($\Delta T/\Delta y=1.5$ °C over a 1.5 mm distance), when compared to 3.5 °C at x_1 due to the slower rate of heat transfer by diffusion.

The temperature profiles and gradients along x and y provide valuable insights into the heat transfer mechanisms during the departure of a bubble. The sharp increase in temperature observed at y_1 =0 indicates the importance of heat transfer from the heated surface and superheated liquid layer to the surrounding liquid. The gradual decrease in temperature observed at x_2 far from the liquid-vapor interface underscores the significant interplay between diffusion and the Marangoni effect in the heat transfer mechanisms.

3.5. Temperature distributions at different planes

We quantified 2D temperature distributions at different z planes, starting from the middle plane of the bubble cross-section (z=0) and

moving toward the positive z-direction at $\Delta z = 0.5$ mm and $\Delta z = 1$ mm, as shown in Fig. 15. At the middle plane (z = 0), the liquid temperature showed a higher average liquid temperature compared to other planes ($\Delta z = 0.5$, and $\Delta z = 1$ mm), indicating higher convective heat transfer from the bubble to the surrounding liquid (the temperature of vapor is higher than the bulk liquid temperature because of heat flux from the heated surface and the superheated liquid layer). The approximate temperature difference at the same x-y locations on the plane at z = 0mm and z = 0.5 mm is measured to be in the range of 3–5 °C. This is expected as the middle plane is where the temperature gradient is most intense with a larger surface area of the bubble in contact with the heated surface and the superheated liquid layer. A much lower average liquid temperature at z = 0.5 mm is presumably because a smaller surface area is in contact with the fluid, and heat transfer becomes restricted. It should be noted that, at the z = 0.5 mm plane, the temperature closer to the liquid-vapor interface will be much higher than

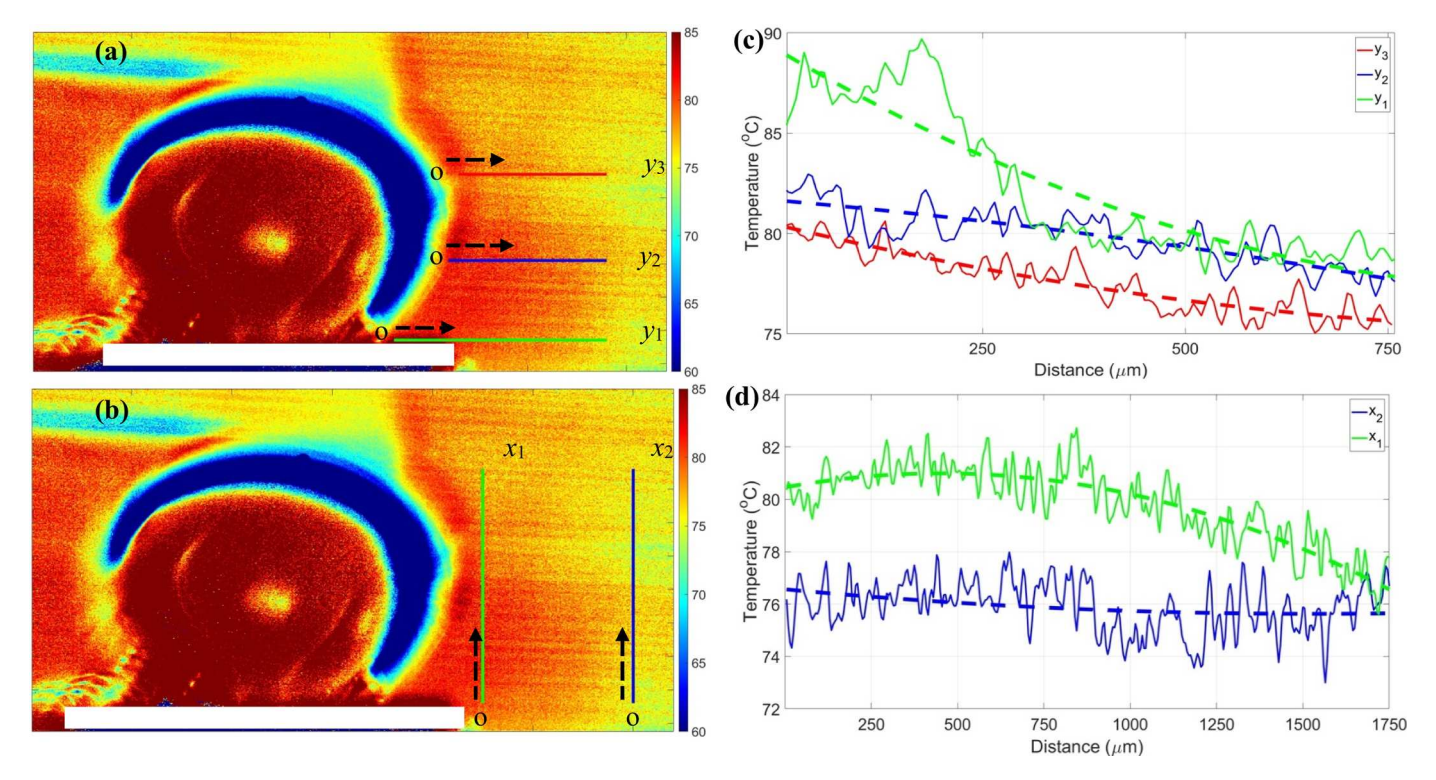


Fig. 14. (a, b) Temperature map surrounding a growing bubble at 10 s after initiation. The lines at different x and y locations are shown to measure temperature profiles. (c, d) Temperature profiles along horizontal lines (y_1 , y_2 , y_3) and vertical lines (x_1 , x_2). Note that the temperature profiles in Fig. 14c are shown from 0 – 750 μ m along y direction, so the lengths of y_1 , y_2 , and y_3 are irrelevant to the actual distance scale in Fig. 14c.

the temperature farther from the interface, due to the temperature gradient (see Fig. 14c). This means, the temperature difference between z=0 mm and z=0.5 mm at the same distance from the liquid-vapor interface would be much larger than 3–5 °C. At $\Delta z=1$ mm, average liquid temperature is significantly lower than that at z=0 and 0.5 mm, which is attributed to the fact that at $\Delta z=1$ mm, the measurement plane is much further away from the heated surface, leading to a lower temperature increase. In sum, the heat transfer magnitude at different z planes varies considerably, resulting in unique temperature gradients from the liquid-vapor interface toward the bulk fluid.

3.6. Heat transfer coefficient using rohsenow correlation

The DFT temperature measurements were used to estimate the heat transfer coefficient associated with the bubble growth. We employed Rohsenow empirical correlation to estimate heat transfer rates, one of the acceptable equations is in a good agreement with experimental measurements [27,28]. In this correlation, the heat transfer coefficient (h) was estimated using physical properties of the liquid, including density ρ_l , specific heat (h), latent heat of vaporization (h), and the diameter of the bubble (h) formed during boiling. Additionally, the correlation includes a dimensionless parameter, h, that characterizes the heat flux and a power exponent, h, that depends on the mode of boiling (1.5 < h), and h is a coefficient that is based on the surface-fluid combination (for copper-water combination = 0.013) [29–31].

$$h = B \cdot \rho_l^{0.5} c_l^{0.5} \left(h_{fg} d \right)^{0.25} \cdot q^{m+0.5} \cdot \Delta T^{m+0.25}$$
(4)

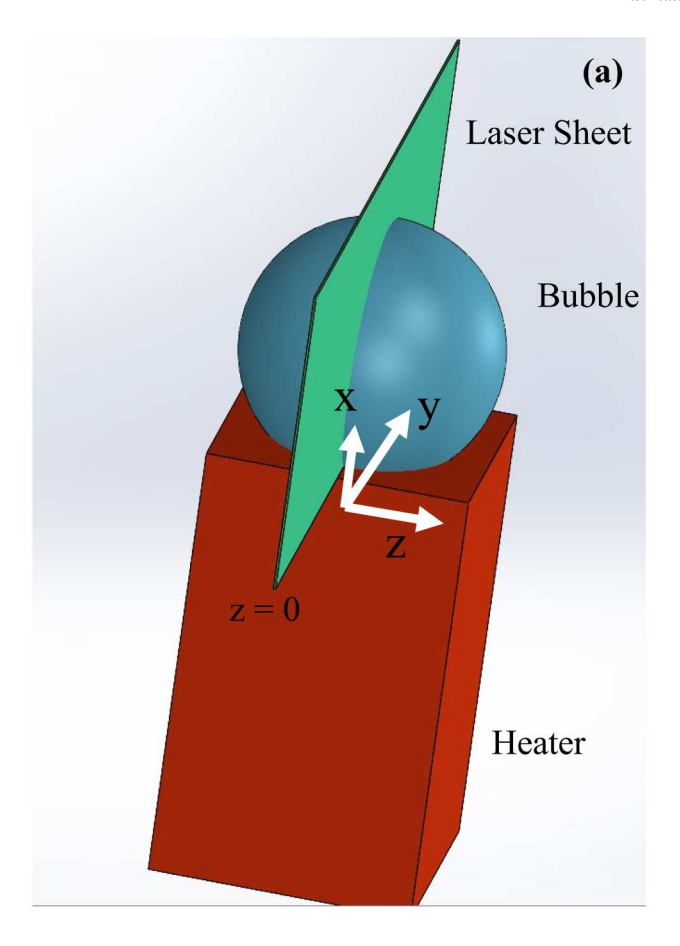
Fig. 16 shows the distribution of heat transfer coefficients around a single bubble and its profile at y_1 , y_2 , and y_3 , estimated by the Rohsenow correlation. Based on these figures, the heat transfer coefficients are higher close to the bubble interface, heated surface, and in the superheated liquid layer. The estimated gradients of convective heat transfer coefficients (Δh) at y_1 , y_2 , and y_3 are 1476 W/m^2K , 519 W/m^2K , and 420 W/m^2K , respectively, for a 0.75 mm distance. These values indicate a

substantial variation in heat transfer coefficients along the horizontal lines, reflecting the spatial distribution of heat transfer around the bubble. In Fig. 16a, we observe that the heat transfer coefficient is higher in proximity to the liquid-vapor interface, the heated surface, and the superheated liquid layer. This observation aligns with our understanding that these regions play a crucial role in heat transfer during bubble departure. The elevated heat transfer coefficient in these areas indicates intensified thermal interaction and enhanced heat dissipation. Furthermore, we found that the heat transfer coefficients close to the liquid-vapor interface and heater are approximately 1.3 times higher than those in the bulk liquid. The heat transfer coefficient near the heated surface is approximately 8% higher than that in the superheated liquid layer.

4. Conclusion

This study aimed to accurately measure the local liquid temperature distributions surrounding a growing bubble during nucleate boiling. Using the DFT technique combined with high-speed imaging, the study measured the 2D, space-and-time-resolved temperature distribution at 10 μm at 0.3 $^{\circ}$ C. The results provide insights into the dominant heat and mass transfer leading to bubble growth and departure. The noteworthy findings are summarized below:

- During bubble growth, liquid temperature is nonuniform near the growing bubble due to the non-uniform heat transfer from the superheated liquid layer and heated surface.
- During departure, liquid temperature shows a transient behavior with rapid temperature rise near the heater and bubble interface just before departure, temperature drop after detachment, and gradually the temperature returns to the pre-bubble state.
- The liquid temperature distribution around a single bubble is highly transient and dependent on different stages of bubble growth and departure. The temperature exhibits a strong transient behavior



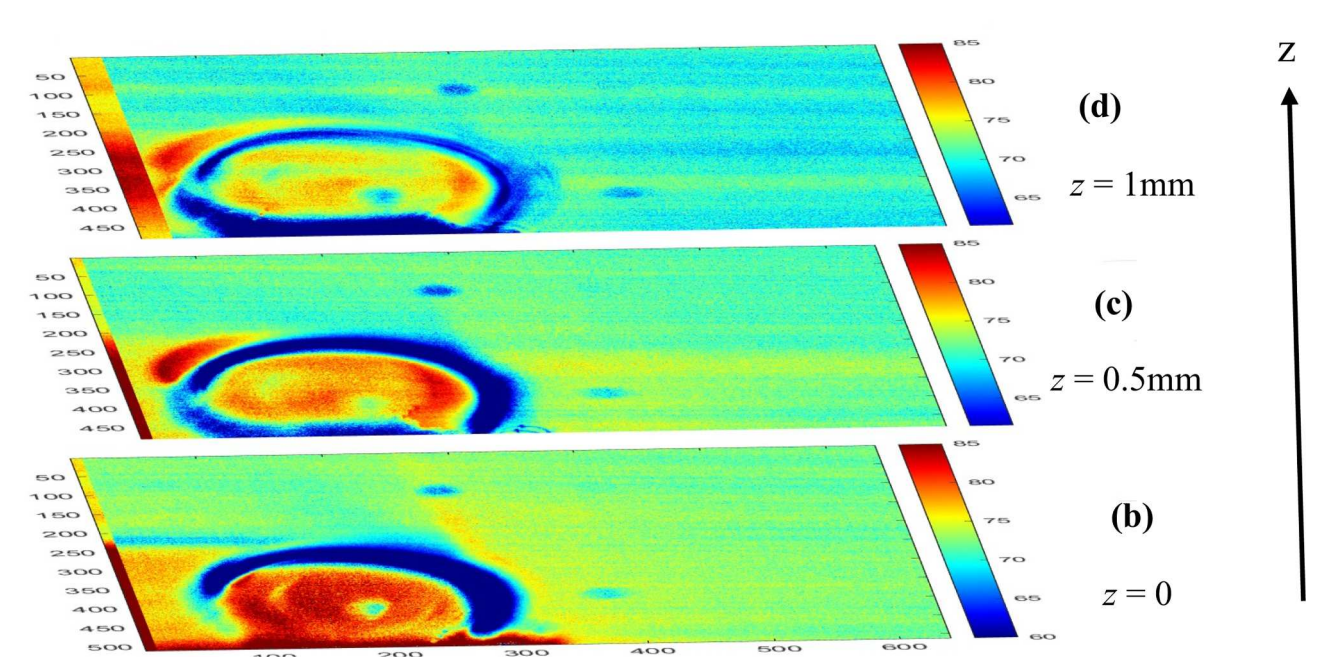
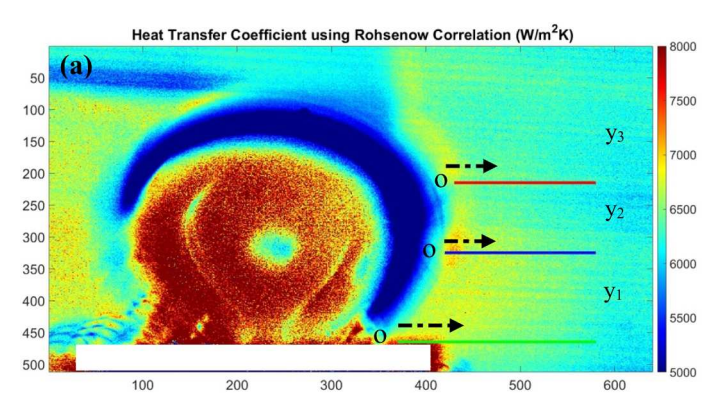


Fig. 15. (a) Schematic of the laser sheet movement along z direction. (b–d) Liquid temperature distributions near a growing bubble at 8 s after initiation at different z locations at (b) z = 0, (c) z = 0.5 mm, and (d) z = 1 mm.

immediately before departure, with a peak temperature difference right before departure and after departure up to 10 $^{\circ}\text{C}$ observed during bubble growth and departure.

- The liquid temperature distribution on different *z* planes reveals that the temperature decreases as the measurement plane moves closer to
- the bubble interface due to the reduced surface area, leading to less efficient heat transfer.
- The temperature and heat transfer measurements in this study provide valuable insights into nucleate boiling, which can be further utilized to optimize the thermal management of extreme heat loads in electrical systems. The findings highlight the highly transient



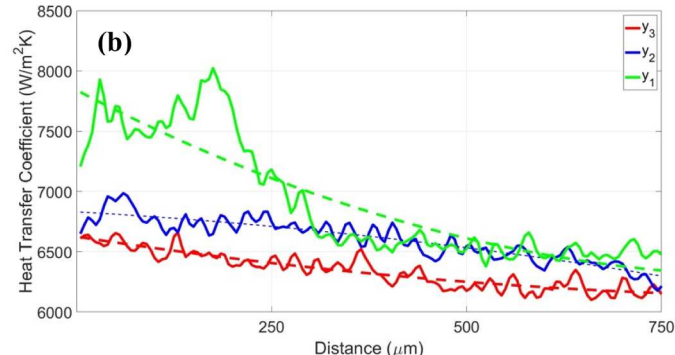


Fig. 16. (a) A distribution of heat transfer coefficients estimated by Rohsenow correlation, and (b) Heat transfer coefficients on horizontal lines at t = 10 s after the bubble initiation.

nature of the temperature distribution around a single bubble at different spatial locations, emphasizing the necessity to accurately measure and account for these dynamic heat transfer characteristics in thermal transport models. Additionally, the comprehensive temperature information obtained in this study can be used to validate existing thermal transport models.

CRediT authorship contribution statement

Mahyar Ghazvini: Conceptualization, Formal analysis, Methodology, Investigation, Writing – original draft, Writing – review & editing. Abel Abraham: Formal analysis, Methodology, Investigation, Writing – review & editing. Mazen Hafez: Conceptualization, Formal analysis, Writing – review & editing. Myeongsub Kim: Conceptualization, Methodology, Supervision, Writing – original draft, Writing – review & editing.

Declaration of competing interest

The authors declare the following financial interests/personal relationships which may be considered as potential competing interests: Myeongsub Kim reports financial support by US National science foundation.

Data availability

Data will be made available on request.

Acknowledgement

This study was financially supported by the National Science Foundation (#1917272).

References

- [1] R. Sharma, T. Farrukh, M. Kim, S. Shirley, M. Kavosi, Microalgae harvesting in a microfluidic centrifugal separator for enhanced biofuel production, in: Proceedings of the ASME 18th International Conference on Nanochannels, Microchannels, and Minichannels, ICNMM, 2020, https://doi.org/10.1115/ICNMM2020-1078. Collocated with ASME 2020 Heat Transf. Summer Conf. ASME 2020 Fluids Eng. Div. Summer Meet.
- [2] M. Ghazivini, M. Hafez, A. Ratanpara, M. Kim, A review on correlations of bubble growth mechanisms and bubble dynamics parameters in nucleate boiling, J. Therm. Anal. Calorim. 2021 (2021) 1–37, https://doi.org/10.1007/S10973-021-10876-2.
- [3] Y.C. Kweon, M.H. Kim, Experimental study on nucleate boiling enhancement and bubble dynamic behavior in saturated pool boiling using a nonuniform de electric field, Int. J. Multiph. Flow 26 (2000) 1351–1368, https://doi.org/10.1016/S0301-9322(99)00090-7.
- [4] M. Khoshvaght-Aliabadi, E. Hosseinirad, M. Farsi, F. Hormozi, Heat transfer and flow characteristics of novel patterns of chevron minichannel heat sink: an insight

- into thermal management of microelectronic devices, Int. Commun. Heat Mass Transf. 122 (2021) 105044, https://doi.org/10.1016/J. ICHEATMASSTRANSFER.2020.105044.
- [5] M. Kim, M. Yoda, Dual-tracer fluorescence thermometry measurements in a heated channel, Exp. Fluids 49 (2010) 257–266, https://doi.org/10.1007/S00348-010-0853-9, 2010 491.
- [6] J. Sakakibara, R.J. Adrian, Measurement of temperature field of a Rayleigh-Bénard convection using two-color laser-induced fluorescence, Exp. Fluids 37 (2004) 331–340, https://doi.org/10.1007/S00348-004-0821-3, 2004 373.
- M. Kim, M. Yoda, The spatial resolution of dual-tracer fluorescence thermometry in volumetrically illuminated channels, Exp. Fluids. 55 (2014) 1–12, https://doi.org/ 10.1007/S00348-013-1649-5/METRICS.
- [8] J.P. Crimaldi, The effect of photobleaching and velocity fluctuations on singlepoint LIF measurements, Exp. Fluids 23 (1997) 325–330, https://doi.org/10.1007/ S003480050117, 1997 234.
- [9] G.W. Walker, V.C. Sundar, C.M. Rudzinski, A.W. Wun, M.G. Bawendi, D.G. Nocera, Quantum-dot optical temperature probes, Appl. Phys. Lett. 83 (2003) 3555, https://doi.org/10.1063/1.1620686.
- [10] J. Coppeta, C. Rogers, Dual emission laser induced fluorescence for direct planar scalar behavior measurements, Exp. Fluids 25 (1998) 1–15, https://doi.org/ 10.1007/S003480050202/METRICS.
- [11] M. Tange, K. Kuribayashi, A. Abdelghany, Temperature measurement around multiple boiling bubbles in a confined space using two-color laser-induced fluorescence, J. Therm. Sci. Technol. 16 (2021) 1–9, https://doi.org/10.1299/ JTST.2021JTST0005.
- [12] V. Voulgaropoulos, G.M. Aguiar, C.N. Markides, M. Bucci, Simultaneous laser-induced fluorescence, particle image velocimetry and infrared thermography for the investigation of the flow and heat transfer characteristics of nucleating vapour bubbles, Int. J. Heat Mass Transf. 187 (2022) 122525, https://doi.org/10.1016/J.JJHEATMASSTRANSFER, 2022, 122525.
- [13] A. Abdelghany, K. Kuribayashi, M. Tange, Ratiometric laser-induced fluorescence for liquid-phase thermometry around boiling bubbles at extended temperatures above 70°C, Exp. Fluids 63 (2022) 1–9, https://doi.org/10.1007/S00348-022-03397-7/METRICS.
- [14] J. Coppeta, C. Rogers, Dual emission laser induced fluorescence for direct planar scalar behavior measurements, Exp. Fluids 25 (1998) 1–15, https://doi.org/ 10.1007/S003480050202, 1998 251.
- [15] M.B. Shafii, C.L. Lum, M.M. Koochesfahani, *In situ* LIF temperature measurements in aqueous ammonium chloride solution during uni-directional solidification, Exp. Fluids 48 (2009) 651–662, https://doi.org/10.1007/S00348-009-0758-7, 2009
- [16] M. Kim, M. Yoda, Fluorescence thermometry for measuring wall surface and bulk fluid temperatures, in: Proceedings of the 14th International Heat Transfer Conference IHTC 4, 2011, pp. 65–74, https://doi.org/10.1115/IHTC14-22884, 14.
- [17] M. Ghazvini, M. Hafez, P. Mandin, M. Kim, Experimental study of bubble growth on novel fin structures during pool boiling, Int. J. Multiph. Flow 168 (2023) 104568, https://doi.org/10.1016/J.IJMULTIPHASEFLOW.2023.104568.
- [18] D. Wang, X. Quan, C. Liu, P. Cheng, An experimental investigation on periodic single bubble growth and departure from a small heater submerged in a nanofluid containing moderately hydrophilic nanoparticles, Int. Commun. Heat Mass Transf. 95 (2018) 1–8, https://doi.org/10.1016/j.icheatmasstransfer.2018.03.016.
- [19] S. Bovard, H. Asadinia, G. Hosseini, S.A. Alavi Fazel, Investigation and experimental analysis of the bubble departure diameter in pure liquids on horizontal cylindrical heater, Heat Mass Transf. 53 (2017) 1199–1210, https://doi. org/10.1007/s00231-016-1885-3. Und Stoffuebertragung.
- [20] H.T. Phan, N. Caney, P. Marty, S. Colasson, J. Gavillet, A model to predict the effect of contact angle on the bubble departure diameter during heterogeneous boiling, Int. Commun. Heat Mass Transf. 37 (2010) 964–969, https://doi.org/10.1016/j. icheatmasstransfer.2010.06.024.
- [21] R.W. Cole-R, Correlation of bubble departure diameters for boiling of saturated liquids, Chem. Eng. Prog. Symp. Ser. 65 (1969) 211–213. https://www.google. com/search?sxsrf=ACYBGNSfkzDC0ycWfeVKf3pMGCgXRate6w%3A1578960 422166&ei=JgYdXvfxCajW5gL1uIHoCA&q=Correlation+of+bubble+departure+

- $\frac{diameters+for+boiling+of+saturated+liquids\&oq=Correlation+of+bubble+departure+diameters+for+boiling+of+satur.\ accessed\ January\ 13,\ 2020.$
- [22] R.E. Eastman, Dynamics of bubble departure, in: AIAA Pap., AIAA, 1984. 10.251 4/6.1984-1707.
- [23] R.L. Mohanty, M.K. Das, A critical review on bubble dynamics parameters influencing boiling heat transfer, Renew. Sustain. Energy Rev. 78 (2017) 466–494, https://doi.org/10.1016/j.rser.2017.04.092.
- [24] Y.J. Chen, K. Ling, S.Q. Jin, W. Lu, B. Yu, D. Sun, W. Zhang, W.Q. Tao, Numerical investigation of critical heat flux during subcooled flow boiling in a vertical rectangular Mini-channel, Appl. Therm. Eng. 221 (2023) 119862, https://doi.org/ 10.1016/J.APPLTHERMALENG.2022.119862.
- [25] L. Cheng, Fundamental issues of critical heat flux phenomena during flow boiling in microscale-channels and nucleate pool boiling in confined spaces, 34 (2013) 1016–1043, 10.1080/01457632.2013.763538.
- [26] Y. Hu, S. Chen, J. Huang, M. Song, Marangoni effect on pool boiling heat transfer enhancement of self-rewetting fluid, Int. J. Heat Mass Transf. 127 (2018) 1263–1270, https://doi.org/10.1016/J.IJHEATMASSTRANSFER.2018.08.003.

- [27] I.L. Pioro, Experimental evaluation of constants for the Rohsenow pool boiling correlation, Int. J. Heat Mass Transf. 42 (1999) 2003–2013, https://doi.org/ 10.1016/S0017-9310(98)00294-4.
- [28] W.M. Rohsenow, H.Y. Choi, Heat, mass, and momentum transfer, (1961).
- [29] M.R. Mohaghegh, A. Raihan, M. Siddique, S. Mahmud, S. Tasnim, A new correlation for the onset of nucleate boiling heat flux under an impinging planar water jet, (2020). 10.11159/ffhmt20.174.
- [30] D.S. Wen, B.X. Wang, Effects of surface wettability on nucleate pool boiling heat transfer for surfactant solutions, Int. J. Heat Mass Transf. 45 (2002) 1739–1747, https://doi.org/10.1016/S0017-9310(01)00251-4.
- [31] I. Nejati, A. Sielaff, B. Franz, M. Zimmermann, P. Hänichen, K. Schweikert, J. Krempel, P. Stephan, A. Martin, H. Scheerer, T. Engler, M. Oechsner, Experimental investigation of single bubble nucleate boiling in microgravity, Microgravity Sci. Technol. 32 (2020) 597–607, https://doi.org/10.1007/S12217-020-09813-Z/METRICS.